Numerical simulations of gyroid structures under compressive loads

R. Miralbes[a]*, J. Cuartero[a], D. Ranz[a] and N. Correia[a]

[a] *Department of Design and Manufacturing, University of Zaragoza, Zaragoza, Spain*

b. Department of Composite Materials, INEGI, Porto, Portugal.

* miralbes@unizar.es. DIDYF-EINA. C/ Maria de Luna n. 4, 50018, Zaragoza (Spain).

Numerical simulations of gyroid structures under compressive loads

Numerical simulations are essential for predicting the mechanical properties of new materials, structures, and final products. In the case of triple periodic minimal surface structures, particularly gyroids, predicting the mechanical behaviors beyond the elastic region is difficult, especially under high strains. This work addresses this issue and introduces a method to predict the mechanical behaviors of gyroid structures using the finite element method. In addition, the mechanical properties of the constitutive material are determined experimentally. Furthermore, different methods are explored, including the use of shell elements, solid elements, and homogenization. Results reveal that homogenization is more suitable for obtaining the properties in the elastic zone, whereas solid models are better for determining the behaviors in the plateau zone and the densification point.

Keywords: gyroid; lattice; numerical; finite elements method; compression; Triple periodic minimal surface.

1. Introduction and literature review

Triple periodic minimal surface (TPMS) structures are lightweight structures generated by unit cells that repeat in different directions. This unit cell is defined by a mathematical equation that ensures the internal surface is minimal; the surfaces are then thickened to generate a solid structure. Consequently, the final structure maximizes the mechanical properties per unit weight[1]. These structures are generated by additive manufacturing (AM) technologies that also use different types of materials, multimaterial configurations[2], graded structures[3] and products with different TPMS configurations depending on the zone. Hence, the possibility of customizing mechanical properties is infinite.

Studies have revealed that these structures can be used as substitutes for other materials such as foams in energy absorption applications (including helmets, bumpers, and good envelopes)[4, 5] or the core of sandwich structures[6].

There are many different types of TPMSs, but the most common are gyroid, diamond, Schwarz-P, Split-P, Neovius, and lidinoid[7]. One of the most studied structures is the gyroid; therefore, this study focuses on this structure. These structures have been

studied mainly under compression and using experimental tools[3–5, 8] in addition, TPMSs under compression have stress–strain curves similar to that of a foam, which was observed and described by Gibson-Ashby, who also identified three well-defined zones that are described subsequently.

Although experimental methods have been extensively used to characterize TPMSs[8, 9], other methods should also be studied to simulate these structures without manufacturing and testing physical prototypes. Because the TPMS stress–strain curve is similar to that described by Gibson-Ashby for foams[10], the Gibson-Ashby material models and their equations have also been used to predict the mechanical properties of solid materials[10]. However, some studies[11, 12] have revealed that the main parameters of the Gibson-Ashby equation must be obtained experimentally. Furthermore, the anisotropy of a TPMS as a function of its internal properties (cell size, thickness of the walls, volume fraction) can predict different mechanical behaviors and undesirable failure modes depending on the load direction[13].

The finite element method (FEM) is another approach for simulating these structures and predicting the mechanical properties and stress–strain curves under compression. There are different approaches for simulating these structures: the simulation of the TPMS using its actual geometry and three-dimensional (3D) shell elements or solid elements[14], the voxel model[15], the super-element model[16] and the simulation of a unit cell and the homogenization process to obtain equivalent mechanical properties for use in the complete structure simulated as a solid, instead of employing the TPMS geometry[17].

Studies by various authors[17–19] have revealed that the homogenization method is useful for determining elastic properties with a relatively low computational cost. Additionally, the equivalent mechanical properties can be used in the simulation of a full-scale product, but only for the elastic properties. Hence, this method can be used to simulate a sandwich structure to predict the stiffness, but this method cannot be used to simulate an impact or to predict the failure or strength[20, 21].

In the case of voxel solids, they can also be used to simulate lattice structures owing to the relatively lower computational cost of solid elements and ease of meshing[21, 22], but there are not many investigations of TPMSs.

Finally, super-elements have not been used[21] in TPMS simulations, although this topic could be interesting.

2. Materials and methods

2.1. Materials

Acrylic styrene acrylonitrile (ASA) manufactured by LEON3D (Leòn, Spain) was used in this study. The experimental specimens were generated with fused filament fabrication (FFF) using a LION 2 printer from LEON3D (Leòn, Spain) with a 4 mm nozzle to print all the specimens with a layer height of 0.19 mm. The material supplier provided some technical data for the material; however, these data were insufficient, thus solid specimens were manufactured and tested under different conditions and printing orientations to analyze the influence of these parameters.

There are many types of TPMS structures, but gyroids are the most studied because of their low anisotropy[13] and high-energy absorption capability per unit mass[4]. This structure has a similar stress–strain curve under compression as a foam and is consistent with the Gibson-Ashby model[10]. TPMS structures are defined by a mathematical equation that describes the 3D surface of a unit cell that repeats along different directions of the specimen. Gyroid structures are defined by Equation 1[23]:

$$\mathrm{F(x,y,z)} = \sin\left(\frac{2\pi x}{a}\right)\cos\left(\frac{2\pi y}{a}\right) + \sin\left(\frac{2\pi y}{a}\right)\cos\left(\frac{2\pi z}{a}\right) + \sin\left(\frac{2\pi z}{a}\right)\cos\left(\frac{2\pi x}{a}\right) - t, \quad (1)$$

where a is the cell size; x, y, and z are the coordinates; and t is a constant adjusted for the desired wall thickness/volume fraction.

There are diverse ways to generate TPMS specimens, but the most common is the generation of the surface of a flat unit cell; afterwards, this process is repeated along different directions to fill the entire volume. In the next stage, the surface is thickened using implicit methods to obtain a solid structure. However, there are some cases that require maintaining the surface structure, such as in numerical simulations with shell elements[17, 24].

Instead of using thickness (t), lattice structures are defined by the volume fraction (ρ^*). ρ^* is the percentage of volume of the solid material (V_{struct}) inside the volume of the structure (V_{solid}) (Equation 2), and this parameter is related to the measured densities of the structure (ρ_{struct}) and solid material (ρ_{solid}).

$$\rho^* = \left(\frac{V_{struct}}{V_{solid}}\right) = \left(1 - \frac{\rho_{struct}}{\rho_{solid}}\right), \quad (2)$$

Consequently, both a and ρ^* are adjustable. In addition, the dimensions of the gyroid specimen to be tested experimentally must be defined. The dimensions of the specimen depend on those defined by the standard employed for the compression experimental test, load capability of the testing machine, and number of unit cells that would be placed inside the specimen. Additionally, the resolution of the printing machine should be considered to obtain a specimen that follows the theoretical shape of the gyroid structure. However, specimens with small unit cells imply that the edge effects influence the mechanical behavior of the structure[19]. Further, specimens with significantly small thicknesses/volume fractions cannot be printed because of the resolution of the printer.

Finally, 40 mm × 40 mm × 40 mm cubic specimens with a unit cell of 10 mm and three volume fractions, 20%, 30%, and 40%, were selected for this study.

The printing orientation could influence the mechanical properties of the final material[8, 25]; thus, cubic specimens were tested in the printing direction that would have higher mechanical properties[25, 26]. In the case of the specimens, the compression specimens were also tested in the layer direction (Z of Fig. 1), but shear and traction were tested under different printing directions (X and Y of Fig. 1). Printing machines have two main printing directions that are usually used in subsequent layers to create 0−90° layers, and the specimens can be reoriented to generate ±45° layers.

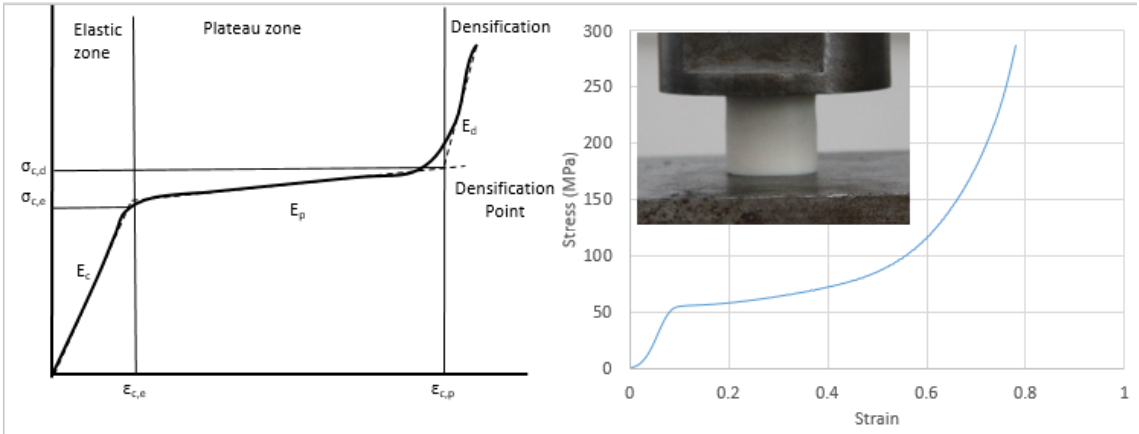

	$\sigma_{c,e}$	$\sigma_{c,d}$	E_c	E_p	E_d	$\varepsilon_{c,e}$	$\varepsilon_{c,d}$
Units	MPa						
	48.6	132.3	923	12.7	1449	0.078	0.635

Fig. 1. Left: typical stress–strain curve of a material that follows the Gibson-Ashby material behavior with the main properties; right: obtained stress–strain curve for acrylonitrile butadiene styrene (ABS). Table: main mechanical properties.

2.2. Methods

Different software can be used to generate the TPMS, such as MATLAB, MathMod, or nTopology. In this study, nTopology (version 3.23.3, New York, NY, USA) was used to generate solid structures and MathMod (version 11.0) was used for the non-thickened structures associated with the shell FEM mesh. Solid structures were used for numerical simulations using solid elements, and printed specimens were used for experimental testing.

2.2.1. Experimental methods

An 8032 Instron uniaxial testing machine (Norwood, MA, USA) with a maximum load capacity of 100 kN and two different load cells (10 kN and 100 kN) was used to test the different specimens at very low velocity to obtain a low strain rate; thus, the results were not influenced by the strain rate. The Instron machine recorded force and displacement, although a strain gauge and an extensometer were also used.

Initially, the solid material was mechanically characterized for use in numerical tests. Consequently, solid material specimens were printed and tested under different pure loads, namely traction, compression, and shear.

In the case involving compression, ASTM D638 was used; therefore, a diameter of 20 mm and height cylinder of 20 mm were tested (see Fig. 1). Using the data obtained from the Instron machine and different dimensions, the stress–strain curve (Fig. 1) and mechanical properties were obtained.

The results (Fig. 1) show that the materials were similar to those detected by Gibson-Ashby[10] for foams with an elastic zone, a plateau, and a densification point, as well as the main mechanical properties. The main mechanical properties are as follows: elastic Young's modulus (E_c), Young's modulus in the plateau (E_p), maximum stress and strain levels in the elastic zone ($\sigma_{c,e}$ and $\varepsilon_{c,e}$) and densification point ($\sigma_{c,p}$ and $\varepsilon_{c,p}$), and average stress in the plateau zone (σ_p).

In the traction test (see Fig. 2), ASTM D638 was used; therefore, bone specimens with the dimensions specified in the standard were used. The material was tested in two printing directions: 0° and 45°. An additional strain gauge from the Instron machine was used to obtain the strain directly. An elastic-plastic stress–strain curve with brittle failure and necking was observed. Different mechanical properties were observed depending on the printing direction: the 0° case had a higher Young's modulus (E_t), but

failure occurred at a lower strain ($\varepsilon_{t,u}$); in the case of 45°, the Young's modulus was lower, but failure occurred at a higher strain. For both cases, the elastic tensile strength ($\sigma_{t,e}$), ultimate tensile strength ($\sigma_{t,r}$), and tensile strength at failure ($\sigma_{t,u}$) were similar. In the case of the ASTM D 5379/D 5379M shear test, two gauges were glued in the middle, and external extensometry acquisition data were used. According to the regulation, these gauges were oriented at an angle of $\pm$45°, but a rosette was used with equivalent directions (see Fig. 3). Three different printing orientations were tested, 0°, 90°, and 45°. The results show that the elastic shear stress (τ_e) and shear modulus (G) were similar; in the case of the ultimate shear strength (τ_u) and ultimate shear strain (γ_u), the 0° and 90° results were similar, but the values for 45° were significantly higher. This difference is due to the optimal configuration to support shear efforts[27]. Finally, the gyroid specimens were tested under compression in the layer direction. There are no specific standards for these structures; however, there are standards for other plastic materials, such as ISO 844, ASTM 3574, and ASTM D1621. These standards are similar but vary in terms of the recommended dimensions of specimens (50 mm × 100 mm × 100 mm prism for ISO 844, 50 mm × 50 mm × 25 mm prism for ASTM 3574, and 25.4 mm × 25.4 mm × 25.4 mm prism for ASTM D1621). Owing to the aforementioned limitations (such as the resolution of the printer, edge effects, and load capability of the Instron machine), we adopted a 40 mm × 40 mm × 40 mm cubic specimen. The internal acquired data of the Instron machine were used to determine the force–displacement and stress–strain curves; additionally, an external camera with an intervalometer was used to capture images of the compression test, which were then compared with the numerical results.

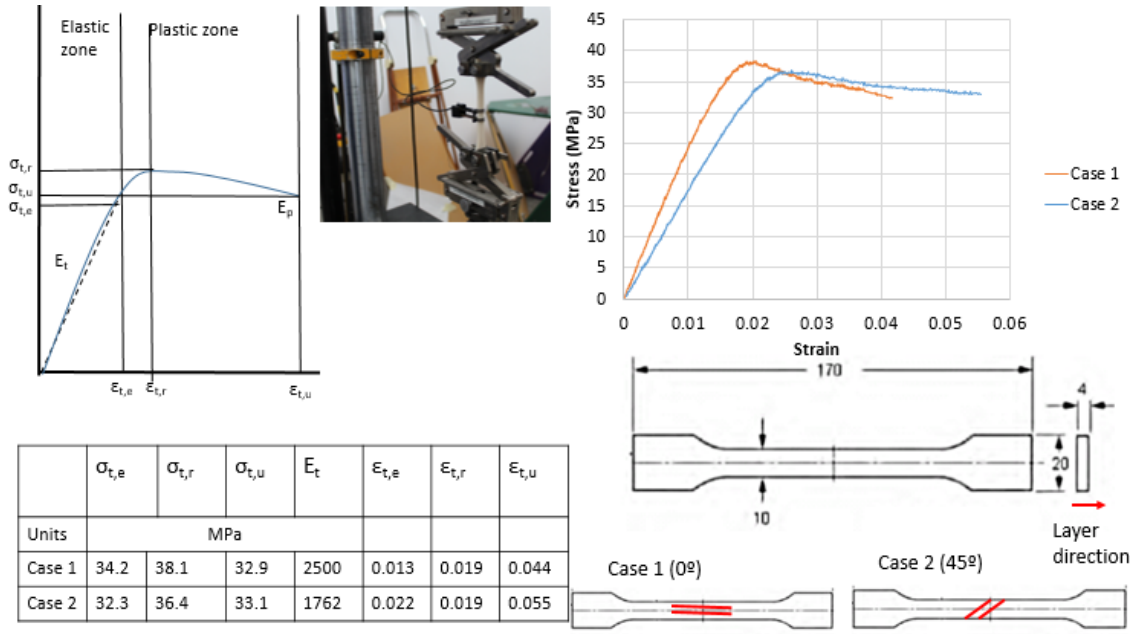

	$\sigma_{t,e}$	$\sigma_{t,r}$	$\sigma_{t,u}$	E_t	$\varepsilon_{t,e}$	$\varepsilon_{t,r}$	$\varepsilon_{t,u}$
Units	MPa						
Case 1	34.2	38.1	32.9	2500	0.013	0.019	0.044
Case 2	32.3	36.4	33.1	1762	0.022	0.019	0.055

Fig. 2. Left: typical stress–strain curve for an elasto-plastic material under compression with the main properties; right: obtained stress–strain curve for acrylonitrile butadiene styrene (ABS). Table: main mechanical properties. Cases: different printing directions.

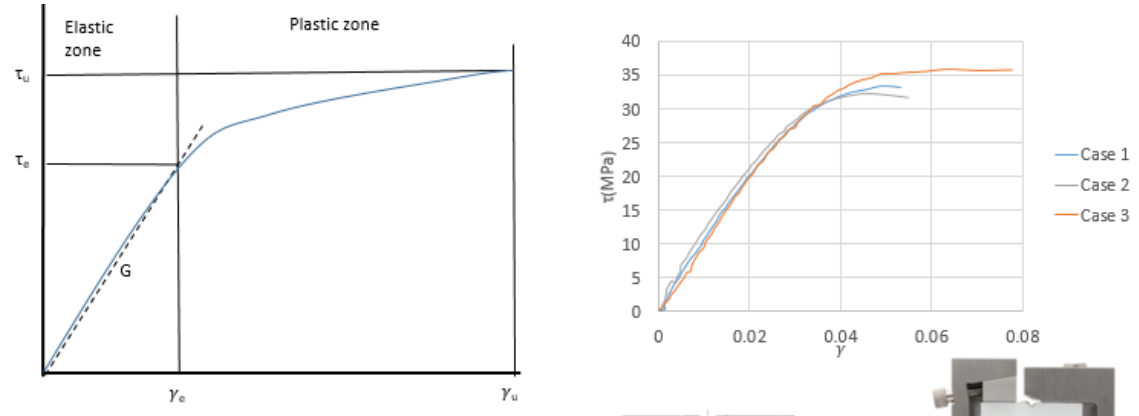

	τ_e	τ_u	G	γ_e	γ_u
Units	MPa				
Case 1	28.3	33.4	1023	0.032	0.053
Case 2	29.1	31.8	1120	0.028	0.054
Case 3	32.3	35.8	1012	0.035	0.077

Fig. 3. Left: typical stress–strain curve for a material under shear with the main properties; Right: obtained stress–strain curve for acrylonitrile butadiene styrene (ABS). Table: main mechanical properties. Cases: different printing directions.

2.2.2. Numerical methods

Different FEM software packages can be used for numerical simulations; here, nTopology and Patran 2021.2 (MSC Software, Newport Beach, CA, USA) were used

for the pre-process, especially to mesh the solid and shell structures, whereas ABAQUS 6.21-6 (Dassault Systèmes, Vélizy-Villacoublay, France) was used for the analysis and post-processing.

The main drawback of the nTopology software is that orthotropic and isotropic materials can only be simulated as elastic materials. Nevertheless, nTopology integrates a homogenization module that enables the simulation of a unit cell under different load cells to obtain the equivalent mechanical properties[19, 20]. Subsequently, a larger structure comprising many of these unit cells can be simulated, without meshing the actual geometry of the structure. In this case, a solid structure was meshed, and equivalent properties were applied. Consequently, with a relatively small number of elements and a low computational cost, the equivalent behavior can be obtained. However, this homogenization method suffers from certain limitations, mainly in that this method is only valid for simulating materials when they are in the elastic zone and that the failure of different elements cannot be predicted. Thus, in the case of a gyroid structure, this method is only valid for simulating the elastic zone of the stress–strain curve. Nevertheless, this method could be useful for simulating, for instance, a sandwich panel with an internal gyroid core to determine its stiffness, although the strength of the structure cannot be predicted. Furthermore, another primary issue is that the mechanical properties introduced in the program (elastic Young's modulus and Poisson's coefficient) vary across the different zones under investigation, and the elastic properties of the material also differ (Fig. 1, Fig. 2, and Fig. 3); in addition, the mechanical properties depend on the printing direction [E_c*:* 923 MPa; E_t*:* 1762 (90°) to 2500 MPa (0°); and *G:* 1023 (0° and 90°) to 1120 MPa (45°)]. A novel study[17, 28–30] has revealed that previous works failed to use the mechanical properties of the solid material in numerical simulations; instead, these simulations employed experimental tests on a lattice structure and inverse engineering to determine the mechanical properties of the numerical model. In certain cases, previous studies have also failed to reveal the values used and/or their precedence[31–36]. Ruiz de Galarreta et al.[37] tested a single strut element under traction to determine the final mechanical properties of a strut lattice structure. Only Al Rifaie[38] used 3D printed solid structures to characterize solid materials under traction (with different printing orientations) and compression (in the layer direction); subsequently, the data were used in the numerical simulations. However, the final mechanical properties of the material in the FEM model were not indicated. In the case of Poisson's coefficient, most researchers employ a value

between 0.3 and 0.35 for acrylonitrile butadiene styrene (ABS) and polylactic acid (PLA)[7, 17, 29, 34, 36, 38, 39].

Thus, the homogenization method was simulated using a 40 mm cubic specimen (Fig. 4), various values for the elastic Young's modulus of the solid material (previously mentioned), and a Poisson's coefficient of 0.3 with nTopology; subsequently, topologic optimization was adopted to obtain the optimized elastic Young's modulus (E_o) using the results of the three different tested specimens. This model can be used to predict the elastic behavior of a material as a function of the volume fraction at a significantly low computational cost. However, the maximum stress in the elastic zone and, consequently, the zones of the stress–strain curves cannot be predicted.

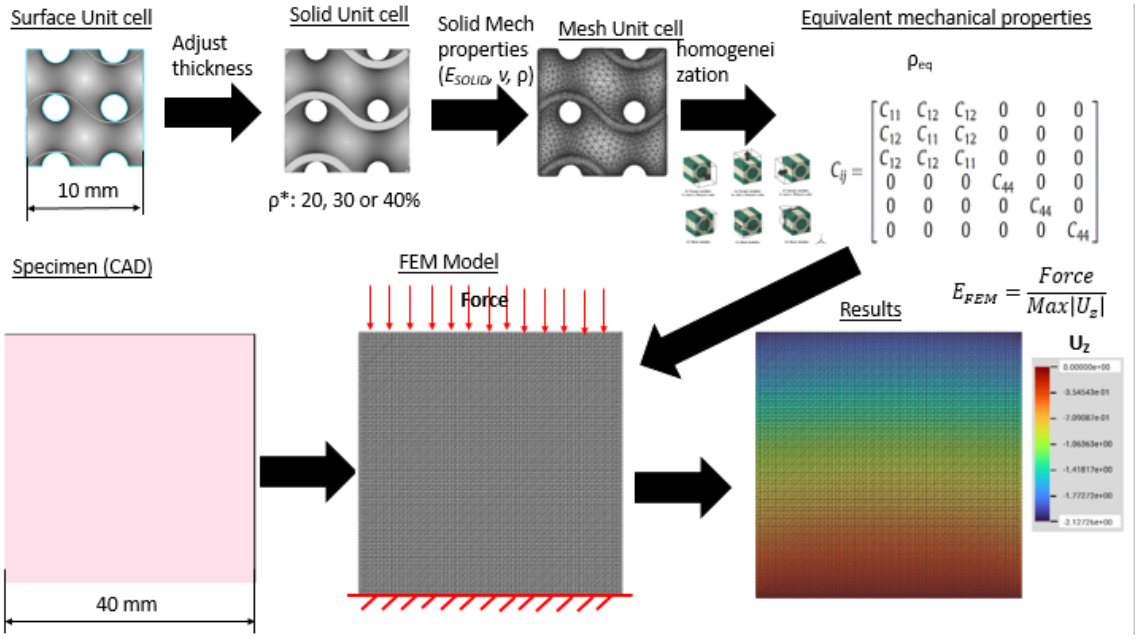

Fig. 4. Scheme of the homogenization process.

Thus, Patran and ABAQUS were used to generate a model of the 40 mm cubic specimen with the real geometry of the gyroids (Fig. 5). Two rigid plates were created to simulate the boundary conditions that were initially at 0.001 mm from the top and bottom of the gyroid structure; one of these plates was completely clamped and the other could only move vertically at a constant velocity (5 mm/min). Hence, a dynamic case with double precision was used to reduce the possible divergences in the results. The material properties and internal contacts should be appropriately defined to simulate the structure. Further, with regard to the contact, a self-contact was used, including rigid walls to simulate both the contact of the internal walls of the gyroid during the crushing process and any part of the gyroid structure with rigid surfaces. These parameters include the recommended internal friction of the contact of 0.1[40].

Additionally, contact control for nodal erosion was included to delete a node of an element-based surface from the general contact domain when all the edges and contact faces to which it is attached have eroded[40].

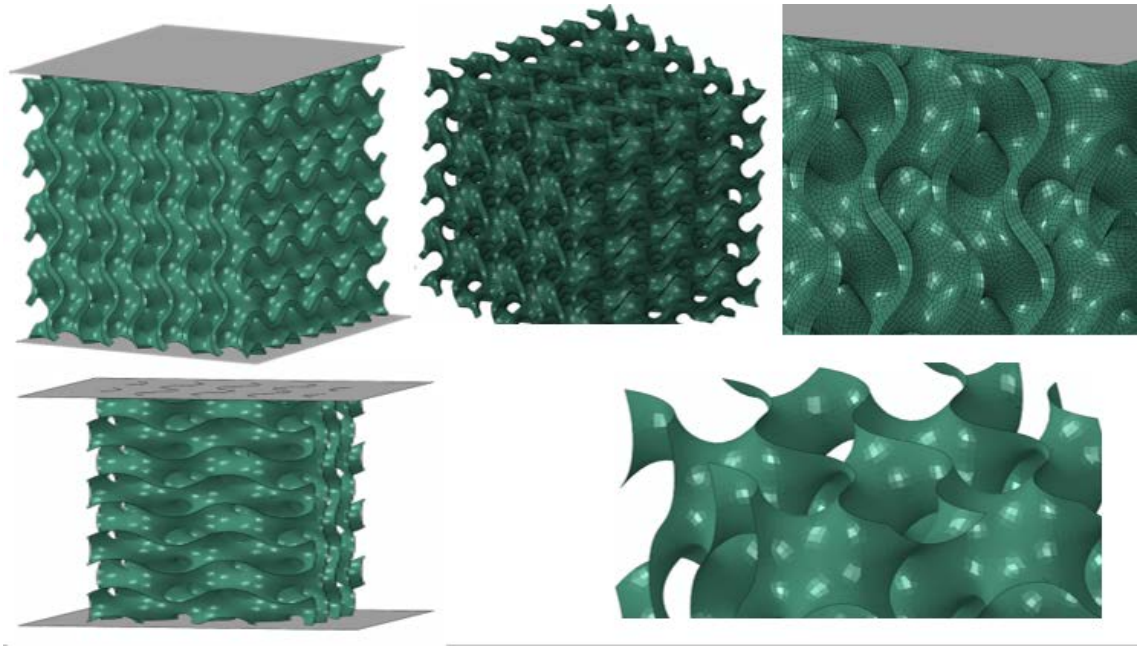

Fig. 5. Solid and shell meshes.

An elastic-plastic material model was used. The elastic modulus of the elastic zone was determined using the value obtained during the topological optimization of the nTopology model. Poisson's coefficient was 0.3, and the density (1150 kg/m^3) was obtained by weighing the solid specimens that were previously tested. The main problem involved determining the different points of the plastic curve. One option could be to use a user material (UMAT) subroutine to define the material properties under traction, compression, and other complex material models. However, this option would render the numerical simulation excessively complex. Consequently, a plastic curve (*plastic) that combines artificial compression and traction was generated. These materials fail under traction or shear stress, mainly with a very low strain. As a result, a combination of the curves was created: if the strain was lower than $\varepsilon_{t,u}$, a traction curve was used, and after this point, with a transition zone and compression curve, the final stress–strain curve can be observed in Fig. 6.

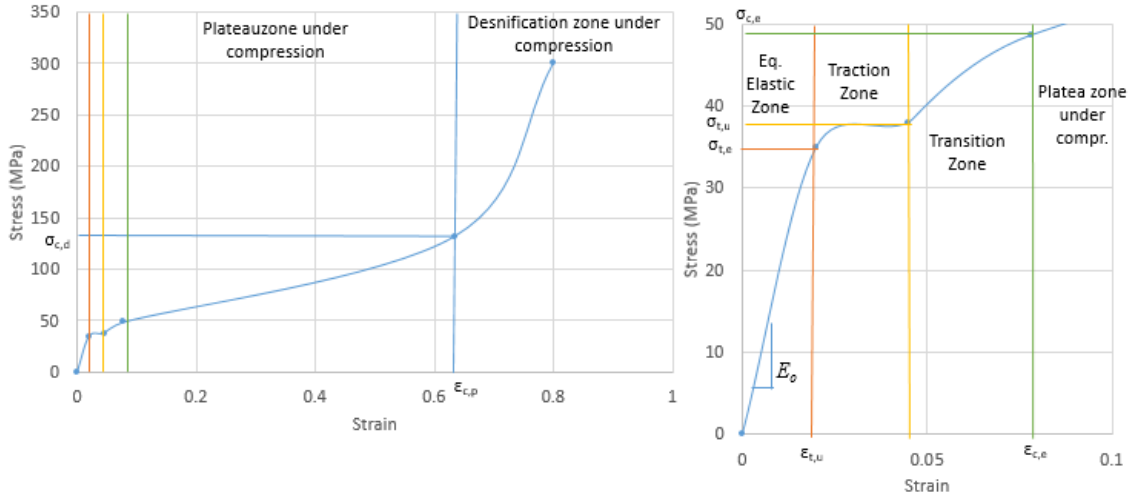

Fig. 6. Stress–strain curve introduced in the finite element method (FEM) to simulate the solid material.

Another aspect was also to simulate failure; in this case, the internal wall of the structure fails mainly due to shear failure. Thus, the result in Fig. 3 (γ_u) was used. However, failure in all directions, as shown in Fig. 2 (*Fail Strain), was realized using the mechanical properties under traction ($\varepsilon_{t,u}$). In the case of compression, however, the structures did not fail; thus, a high value was used (0.99) to avoid failure. Initially, the orientation of the fiber in the structure was unknown, but a 0° orientation (case 1) was more suitable due to manufacturing, thus 5.3% was selected.

Initially, a quarter model was considered to reduce the numerical cost and processing time, but the non-symmetry of the gyroid structure rendered this option impossible. This aspect could be used in other TPMS structures, such as Schwarz-P and Neovius structures.

Similarly, linear shell elements (S4R and S3R) with reduced integration and five integration points in thickness were used; these were standard large-strain shell elements. The dimensions of the gyroid (in relation to the thickness) and curvature of the surface prevented its use. However, the lower number of elements (24578) and nodes needed (23478) to mesh the structure and low computational cost enabled shell models to be used. In addition, shell models allowed the volume fraction to be easily changed without the necessity of re-meshing by changing only the associated thickness of the shell elements.

Additionally, another solid model was developed for comparison with the shell models and experimental results. In this case, a completely different mesh was generated for

each volume fraction. Furthermore, to adequately simulate walls under shear[40, 41], the mesh should have at least four elements in the thickness direction. In addition, elements should not be significantly distorted initially, especially if they would suffer high deformation; therefore, a mesh with a high number of nodes (around 920000) and elements (around 750000) was required. These requirements imply a high computational cost. A general-purpose brick element (C3D8R) with reduced integration was selected to increase the computational efficiency[40]. Additionally, a new mesh was generated for each volume fraction, which implies a higher meshing cost.

3. Results and discussion

Analysis of the results shows that the studied structures follow the Gibson-Ashby prediction for foams; consequently, a higher volume fraction was associated with higher levels of stress and Young's modulus, but also a lower strain at the densification point.

3.1. Homogenization analysis

A comparative analysis of the Young's modulus of the 40 mm cubic gyroid specimen obtained experimentally and numerically using the homogenization process is shown in Table 1. Five different Young's moduli of the constitutive material were obtained from different experimental tests for three different volume fractions (between 923 and 2500 MPa), and the main conclusion is that while none of the materials offers a sufficiently low deviation for all the volume fractions, the equivalent Young's modulus must be in this range of values. As a result, topological optimization was carried out to determine this parameter while minimizing the error; 1560 MPa was the optimal value.

ρ*	E_{solid}	E_{exp}	E_{MEF}	Deviation
%	MPa			%
20	923	73.67	50.49	-31.46
	1762		96.39	30.84
	2500		136.76	85.64
	1023		55.96	-24.04
	1120		61.27	-16.83
	1560		85.34	15.84
30	923	138.25	85.02	-38.51
	1762		162.30	17.39
	2500		230.27	66.56
	1023		94.23	-31.84
	1120		103.16	-25.38
	1560		143.69	3.93
40	923	245.97	126.05	-48.75
	1762		240.63	-2.17
	2500		341.41	38.80
	1023		139.71	-43.20
	1120		152.95	-37.82
	1560		213.04	-13.39

Table 1: Numerical results of the elastic Young's modulus obtained using the homogenization process and experiments.

This value was subsequently used for numerical simulations using shell and solid elements. In Table 2, weights of the different models and small deviations for all models are shown. The theoretical weight calculated using the density of the solid material provided by the manufacturer was usually higher than that obtained using AM.

Weight (g)	20%	30%	40%
Theoric	14.8	22.2	29.6
Experimental	14.7	22.1	29.4
Homogenization	14.4	21.5	28.5
Shell	15.3	22.9	30.6
Solid	15.0	22.5	30.1

Table 2: Final weight of the different finite element method (FEM) models, theoretical models, and those obtained with computer-aided design (CAD) tools.

3.2. Shell element analysis

The results show (see Table 1 and Fig. 7) that the shell model had a higher stiffness in the elastic zone than the experimental model for all volume fractions. Additionally, densification occurred with higher deformation (higher displacement). This densification is because of the failure to control this mode. In the solid models that had at least four elements, failure occurred when the elements disappeared

progressively; in the case of the shell models, the whole element disappeared. Thus, these elements could not contact the opposite wall properly; consequently, the deformation was higher. The stress levels were smaller than those of the solid model and experimental results; additionally, this model could not be used to predict densification. Finally, the shapes of the curves (Fig. 7) were significantly different.

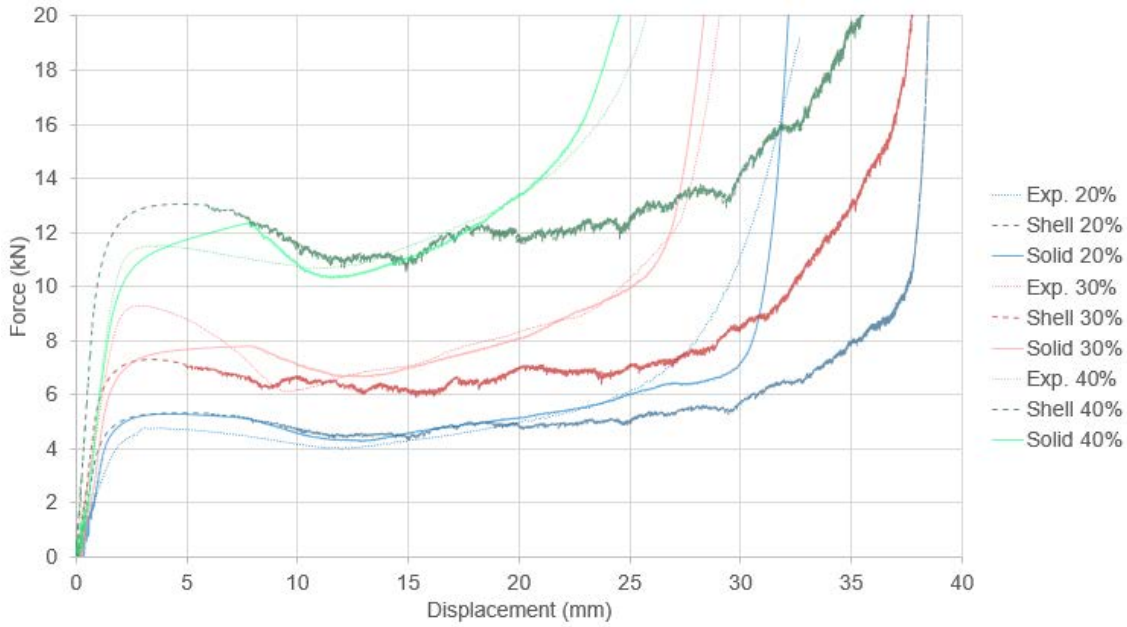

Fig. 7. Obtained stress–strain curve using numerical tools and experimental ones for different volume fractions.

3.3. Solid element analysis

Fig. 7 and Table 3 show that the solid models had high accuracy. The elastic Young's modulus was predicted with low error; under volume fractions of 30% and 40%, the densification point and stress levels in the plateau were also predicted. Owing to the proposed material model and failure values, solid models, as well as shell models, featured an initial peak in the first zone of the plateau; the model values approached the experimental ones as the stress decreased. In the case of the volume fraction of 30%, an initial peak appeared after the elastic zone, which could not be predicted by the solid or shell numerical model. In the case of the volume fraction of 20%, densification appeared with a lower deformation. In the case of the densification zone, the slope was similar for the solid simulation and the experiment; however, under a volume fraction of 20%, a higher step was observed for the solid model. Analyses of the deformation process (see Fig. 8) indicate similar deformations in the numerical and experimental results. The model predicted the layer that initially fails for all the volume fractions and

the layer failure progression. Consequently, the solid model could predict zones with higher levels of stress, which are likely to collapse earlier. A solid mesh included at least four elements comprising the thickness of the gyroid; thus, the failure was not as abrupt as in the case of the shell structure if only one element of the thickness disappeared.

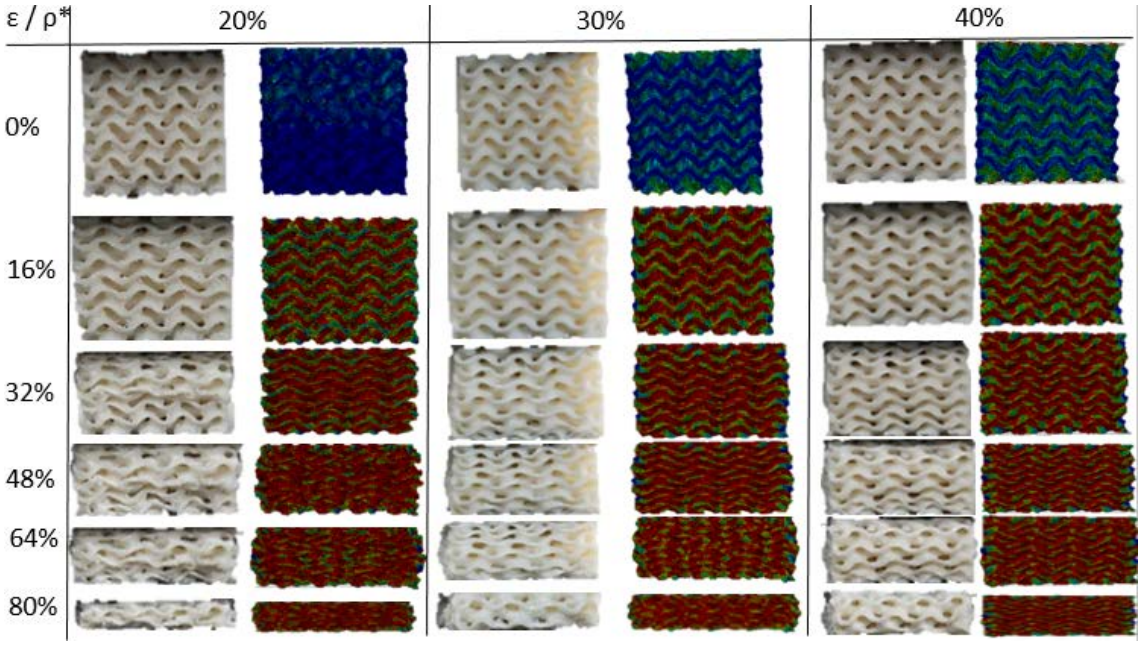

Fig. 8. Comparative study of the deformation process of solid elements by the finite element method (FEM) model and experimental results for different volume fractions.

ρ* (%)		E(MPa)	$\sigma_{c,e}$ (MPa)	σ_p (MPa)	$\sigma_{c,d}$ (MPa)	$\varepsilon_{c,d}$ (%)
20	Exp	73.7	4.4	4.2	6.2	70.2
	Hom	85.4				
	Shell	96.3	4.7	4.6	6.4	78.3
	Solid	84.2	4.7	4.6	6.7	93.2
30	Exp	138.3	6.2	7.7	10.5	62.5
	Hom	143.7				
	Shell	167.8	8.8	6.4	8.6	82.5
	Solid	121.4	6.5	7.2	10.2	63.2
40	Exp	246	10.8	11.1	14.1	54.3
	Hom	213				
	Shell	267	9.9	11.9	16.3	76.6
	Solid	254	11.2	11.4	14.6	57.2

Table 3: Mechanical properties obtained using the finite element method (FEM) and experiments.

4. Conclusions

The conclusions of this work can be summarized as follows. The while solid and homogenization numerical models exhibited sufficient accuracy in terms of determining Young's modulus, although the homogenization method achieved better performance owing to its lower computational cost and CPU time. In the case of the shells, the results were significantly higher. However, homogenization failed to predict the strength of the structure and the behavior in the plateau and densification zones.

Although the shell element model could approximate the levels of stress in the plateau zone, this model could not adequately predict the appearance of the densification point with a much higher deformation; therefore, this model was inadequate for this purpose, despite the lower computational cost and CPU time than those of the solid numerical model.

The solid numerical model performed better in terms of simulating the behavior of the gyroid structure; however, the corresponding computational cost and CPU time reduce its applicability. Consequently, for a complex product, the number of elements and the CPU time would be excessive; therefore, another method should be developed. The proposed material model simulated these structures using the mechanical properties of the solid material alone. Therefore, the elastic Young's modulus required further adjustments.

Finally, owing to the CPU time cost, computational effort, and difficulties in meshing complex products with solid elements, the solid models were not adequate for simulating products with a significant number of gyroid unit cells. Consequently, different simulation methods are necessary to simulate gyroid structures. Currently, one possible solution is a UMAT subroutine; therefore, instead of a mesh of the actual structure of a gyroid, the structure could be meshed as a solid without holes. This compromise implies fewer elements (similar to the homogenization method), which, in turn, would imply a simpler pre-process stage and a considerably lower processing time. Another possible solution is the use of super-elements and multiscale models.

5. References

1. Guo X, Zheng X, Yang Y, et al (2019) Mechanical behavior of TPMS-based scaffolds: a comparison between minimal surfaces and their lattice structures. SN Appl Sci 1:1145. https://doi.org/10.1007/s42452-019-1167-z

2. Callens SJP, Arns CH, Kuliesh A, Zadpoor AA (2021) Decoupling Minimal Surface Metamaterial Properties Through Multi-Material Hyperbolic Tilings. Adv Funct Mater 31:2101373. https://doi.org/10.1002/adfm.202101373

3. Miralbes R, Higuera S, Ranz D, Gomez JA (2021) Comparative analysis of mechanical properties and energy absorption capabilities of functionally graded and non-graded thermoplastic sheet gyroid structures. Mech Adv Mater Struct 1–14. https://doi.org/10.1080/15376494.2021.1949509

4. Miralbes R, Ranz D, Pascual FJ, et al (2020) Characterization of additively manufactured triply periodic minimal surface structures under compressive loading. Mech Adv Mater Struct 1–15. https://doi.org/10.1080/15376494.2020.1842948

5. Higuera S, Miralbes R, Ranz D (2021) Mechanical properties and energy–absorption capabilities of thermoplastic sheet gyroid structures. Mech Adv Mater Struct 1–15. https://doi.org/10.1080/15376494.2021.1919803

6. Fashanu O, Rangapuram M, Abutunis A, et al (2022) Mechanical performance of sandwich composites with additively manufactured triply periodic minimal surface cellular structured core. J Sandw Struct Mater 24:1133–1151. https://doi.org/10.1177/10996362211037012

7. Krishnan K, Lee D-W, Al Teneji M, Abu Al-Rub RK (2022) Effective stiffness, strength, buckling and anisotropy of foams based on nine unique triple periodic minimal surfaces. Int J Solids Struct 238:111418. https://doi.org/10.1016/j.ijsolstr.2021.111418

8. Silva C, Pais AI, Caldas G, et al (2021) Study on 3D printing of gyroid-based structures for superior structural behaviour. Prog Addit Manuf 6:689–703. https://doi.org/10.1007/s40964-021-00191-5

9. Yang L, Yan C, Cao W, et al (2019) Compression–compression fatigue behaviour of gyroid-type triply periodic minimal surface porous structures fabricated by selective laser melting. Acta Mater 181:49–66. https://doi.org/10.1016/j.actamat.2019.09.042

10. Gibson LJ, Ashby MF (1997) Cellular Solids: Structure and Properties, 2nd ed. Cambridge University Press

11. Jiang P, De Meter EC, Basu S (2021) The influence of defects on the elastic response of lattice structures resulting from additive manufacturing. Comput Mater Sci 199:110716. https://doi.org/10.1016/j.commatsci.2021.110716

12. Maconachie T, Tino R, Lozanovski B, et al (2020) The compressive behaviour of ABS gyroid lattice structures manufactured by fused deposition modelling. Int J Adv Manuf Technol 107:4449–4467. https://doi.org/10.1007/s00170-020-05239-4

13. Khaleghi S, Dehnavi FN, Baghani M, et al (2021) On the directional elastic modulus of the TPMS structures and a novel hybridization method to control anisotropy. Mater Des 210:110074. https://doi.org/10.1016/j.matdes.2021.110074

14. Maskery I, Aremu AO, Parry L, et al (2018) Effective design and simulation of surface-based lattice structures featuring volume fraction and cell type grading. Mater Des 155:220–232. https://doi.org/10.1016/j.matdes.2018.05.058

15. Aremu AO, Maskery I, Tuck C, et al (2014) A COMPARATIVE FINITE ELEMENT STUDY OF CUBIC UNIT CELLS FOR SELECTIVE LASER MELTING. In: Solid freeform fabrication proceedings,. pp 1238–1249

16. Storm J, Ranjbarian M, Mechtcherine V, et al (2019) Modelling of fibre-reinforced composites via fibre super-elements. Theor Appl Fract Mech 103:102294. https://doi.org/10.1016/j.tafmec.2019.102294

17. Bean P, Lopez-Anido RA, Vel S (2022) Numerical Modeling and Experimental Investigation of Effective Elastic Properties of the 3D Printed Gyroid Infill. Appl Sci 12:2180. https://doi.org/10.3390/app12042180

18. Li D, Liao W, Dai N, et al (2018) Optimal design and modeling of gyroid-based functionally graded cellular structures for additive manufacturing. Comput-Aided Des 104:87–99. https://doi.org/10.1016/j.cad.2018.06.003

19. Jíra A, Šejnoha M, Krejčí T, et al (2021) Mechanical Properties of Porous Structures for Dental Implants: Experimental Study and Computational Homogenization. Materials 14:4592. https://doi.org/10.3390/ma14164592

20. Nasirov A, Fidan I (2020) Prediction of mechanical properties of fused filament fabricated structures via asymptotic homogenization. Mech Mater 145:103372. https://doi.org/10.1016/j.mechmat.2020.103372

21. Simsek U, Akbulut A, Gayir CE, et al (2021) Modal characterization of additively manufactured TPMS structures: comparison between different modeling methods. Int J Adv Manuf Technol 115:657–674. https://doi.org/10.1007/s00170-020-06174-0

22. Downing D, Jones A, Brandt M, Leary M (2021) Increased efficiency gyroid structures by tailored material distribution. Mater Des 197:109096. https://doi.org/10.1016/j.matdes.2020.109096

23. Shoen A (1970) Infinite periodic minimal surfaces without self-intersection

24. Wang Y, Ren X, Chen Z, et al (2020) Numerical and experimental studies on compressive behavior of Gyroid lattice cylindrical shells. Mater Des 186:108340. https://doi.org/10.1016/j.matdes.2019.108340

25. Ramos H, Santiago R, Soe S, et al (2022) Response of gyroid lattice structures to impact loads. Int J Impact Eng 164:104202. https://doi.org/10.1016/j.ijimpeng.2022.104202

26. Gonabadi H, Yadav A, Bull SJ (2020) The effect of processing parameters on the mechanical characteristics of PLA produced by a 3D FFF printer. Int J Adv Manuf Technol 111:695–709. https://doi.org/10.1007/s00170-020-06138-4

27. Rohde S, Cantrell J, Jerez A, et al (2018) Experimental Characterization of the Shear Properties of 3D–Printed ABS and Polycarbonate Parts. Exp Mech 58:871–884. https://doi.org/10.1007/s11340-017-0343-6

28. Smith M, Guan Z, Cantwell WJ (2013) Finite element modelling of the compressive response of lattice structures manufactured using the selective laser melting technique. Int J Mech Sci 67:28–41. https://doi.org/10.1016/j.ijmecsci.2012.12.004

29. Zhang C, Zheng H, Yang L, et al (2022) Mechanical responses of sheet-based gyroid-type triply periodic minimal surface lattice structures fabricated using selective laser melting. Mater Des 214:110407. https://doi.org/10.1016/j.matdes.2022.110407

30. Ramos H, Santiago R, Alves M, et al (2019) Finite element modeling of gyroid structures subjected to impact loadings. In: Proceedings of the 7th International Symposium on Solid Mechanics. ABCM

31. Abueidda DW, Elhebeary M, Shiang C-S (Andrew), et al (2019) Mechanical properties of 3D printed polymeric Gyroid cellular structures: Experimental and finite element study. Mater Des 165:107597. https://doi.org/10.1016/j.matdes.2019.107597

32. Abueidda DW, Bakir M, Abu Al-Rub RK, et al (2017) Mechanical properties of 3D printed polymeric cellular materials with triply periodic minimal surface architectures. Mater Des 122:255–267. https://doi.org/10.1016/j.matdes.2017.03.018

33. Caiazzo F, Guillen DG, Alfieri V (2021) Simulation of the Mechanical Behaviour of Metal Gyroids for Bone Tissue Application. Materials 14:4808. https://doi.org/10.3390/ma14174808

34. León-Becerra J, González-Estrada OA, Quiroga J (2021) Effect of Relative Density in In-Plane Mechanical Properties of Common 3D-Printed Polylactic Acid Lattice Structures. ACS Omega 6:29830–29838. https://doi.org/10.1021/acsomega.1c04295

35. Pouya C, Overvelde JTB, Kolle M, et al (2016) Characterization of a Mechanically Tunable Gyroid Photonic Crystal Inspired by the Butterfly *Parides Sesostris*. Adv Opt Mater 4:99–105. https://doi.org/10.1002/adom.201500436

36. Juarez CZJ, Koay SC, Chan MY, et al (2021) Finite Element Analysis Study on Lattice Structure Fabricated Recycled Polystyrene from Post-used Styrofoam

Waste. MATEC Web Conf 335:03007. https://doi.org/10.1051/matecconf/202133503007

37. Ruiz de Galarreta S, Jeffers JRT, Ghouse S (2020) A validated finite element analysis procedure for porous structures. Mater Des 189:108546. https://doi.org/10.1016/j.matdes.2020.108546

38. Al Rifaie MJ (2021) RESILIENCE AND TOUGHNESS BEHAVIOR OF 3D-PRINTED POLYMER LATTICE STRUCTURES: TESTING AND MODELING. University of Mosul

39. Alwattar TA, Mian A (2020) Developing an Equivalent Solid Material Model for BCC Lattice Cell Structures Involving Vertical and Horizontal Struts. J Compos Sci 4:74. https://doi.org/10.3390/jcs4020074

40. Smith M (2021) ABAQUS/Standard User's Manual, Version 6.21.3. Dassault Systems, USA

41. Ma A, Zhou C, Wang X (2005) Patran he Nastran you xian yuan fen xi zhuan ye jiao cheng. Qing hua da xue chu ban she, Beijing